European Southern Observatory
Organisation Européenne pour des Recherches Astronomiques dans l'Hémisphère Austral
Europäische Organisation für astronomische Forschung in der südlichen Hemisphäre

VLT PROGRAMME

Very Large Telescope

Absolute Photometry with FORS

The FORS Absolute Photometry Project

W. Freudling, M. Romaniello, F. Patat, P. Møller, E. Jehin, K. O'Brien

VLT-TRE-ESO-13100-4006

Issue: 1.1

Issue date: 11.07.2006

Prepared: W. Freudling .....
Name Date Signature

Approved: K. O'Brien .....
Name Date Signature

Approved: E. Jehin .....
Name Date Signature

Released: A. Kaufer .....
Name Date Signature

VLT PROGRAMME ⋆ Telephone: +49-89-32006-0 ⋆ Fax: +49-89-3202362

CHANGE RECORD

ISSUE	DATE	SECTION/PAGE AFFECTED	REASONS/INITIATION DOCUMENTS/REMARKS
1.0	06.07.2006	all	new document
1.1	11.07.2006	all	typos fixed

Contents

1 Executive Summary and Recommendations

The "*FORS Absolute Photometry" (FAP)* project has investigated the feasibility of reaching an absolute photometric accuracy of 3 percent in the R band with the FORS1 camera. The goal of *FAP* was to establish procedures for ESO, and guidelines to observers, on how to systematically achieve this level of accuracy. A total of 4 hours of night time observations were used for this project. The main results are as follows.

Three percent photometric accuracy with FORS1 can be achieved with moderate effort. ESO can help observers to achieve this goal by providing appropriate advice to users and by implementing a scheme for service mode observers to request that observations of an appropriate number of standard star fields are taken. We propose a modification of the calibration procedure to improve the accuracy of routinely obtained photometric zero points. In addition, we suggest some small changes to the QC pipeline that would help observers to improve photometric calibration of observations using the existing calibration plan.

The specific advice derived from the current project is listed below. All conclusions have been derived by analysing FORS1 data, but they probably equally apply to FORS2.

- Advice to all users of FORS:
  - The "master flats" which are the mean of all twilight flats for that night and are created each night by the pipeline, include features which depend on the rotator angle at which the flatfields were taken. These features have amplitudes of up to 5 percent and might result in artifacts in the image of the sky background.
  - Flat fields taken at different times differ significantly from each other. If the background of a science image does not appear to be flat, it might be possible to improve the results by using a different set of flats.
  - The accuracy of relative photometry using the pipeline-produced master flats is about 5 percent peak-to-peak.
  - The absolute zero point computed by the QC pipeline for each night is accurate to about 0.1 mag.
- Advice to Photometric Programmes which need better than 5 percent relative or absolute photometric calibration:
  - There are significant features in the pipeline-produced master flats which lead to photometric errors of up to 5 percent in the R-band. The master flats can be improved by removing the large scale variations. In addition, a 2nd order flat field correction has to be applied for percent-level relative photometric accuracy.
  - Selected regions within the Stetson standard fields contain a sufficient number of standard stars which are faint enough to be used with 10 second integrations.
  - A rule of thumb is that with 3 observations of Stetson standard fields well separated in airmass, zero point accuracy of about 1 percent can be achieved.
  - The "VLT Astronomical Site Monitor" (ASM) is a useful tool to judge the quality of a night and should be consulted.
- Recommendations to ESO:
  - Implement a clear procedure for service observation to request photometric standards taken at three or more different airmasses. A specific proposal is given in Sec. 8.2.

- Obtain images of photometric standard fields for at least two different airmasses in each photometric night. A specific procedure is proposed in Sec. 8.1.
- Use the Stetson fields as photometric standards, and systematically introduce offsets between standard observations as described in Sec. 8.1.
- Use the accumulated data to derive 2nd order flat field correction frames for all broad-band filters in regular intervals.
- Once enough data have accumulated, investigate the stability of the 2nd order correction. Investigate whether flatfielding can be improved by using a new kind of master flat which is updated only occasionally as opposed to using the nightly twilight flats.
- Determine the extinction coefficient for all photometric nights.
- In nights where observations of photometric standards are available for only one airmass, compute the extinction coefficient *assuming* the zero point has not changed from previous nights. The rational is discussed in Sec. 7.2. This could be done in addition to the current procedure of computing zero points assuming the extinction coefficient did not change.
- When zero points are computed assuming the extinction coefficients, list the airmass of standard stars used to derive those zero points.
- Make R-band sensitivity correction frame derived in Sec. 5.3.2 available to observers. To the best of our knowledge, these large scale corrections are stable in time and improve the flatfield. For other filters, make 2nd order corrections available to observers as soon as possible after they have been produced.
- Investigate the origin of the rotating feature on the twilight flats. The feature is described in Sec. 3.2.2. A possible explanation for this feature is scattered light by the guide probe.
- Improve documentation and advertisement for the ASM.
- Review the current way of evaluating the photometric quality of a night to determine, whether the requested data quality has actually been achieved.

If implemented, these small changes in procedures should benefit all FORS programmes which use ESO's published photometric zero points, as well as programmes which require higher photometric accuracy.

2 Introduction

The standard ESO procedure for imaging observations is to obtain images of standard stars with every imaging camera and filter used during that night. These data are taken for the purpose of instrument monitoring, but also serve as a base-line calibration. The calibration goal for photometry is about 5 to 10 percent. This goal is sufficient for the majority of programmes currently carried out with most imaging cameras. Some observers need better accuracy and therefore have to devise their own calibration observations. The requirements of such observers fall in one of two categories.

- Intermediate accuracy uses calibration that can routinely be achieved but requires some extra effort on the part of both the observer and the observatory. For optical photometry, this would be 1 to 3 percent accuracy. The observatory can provide the tools and knowledge to help observers to achieve this.
- Extreme accuracy (better than 1 percent photometry) might be possible to achieve by ambitious teams, which carry out the observations themselves (no service observations). It is clear that the observatory cannot guarantee or play an active role in such programmes. Those teams will need to build own their calibration tools.

For photometric observations in service mode, ESO currently supports only standard calibration. A procedure how to obtain intermediate quality photometric calibration has so far not been established. In order to be able to advise observers who desire to obtain such accuracy, we have carried out a programme to test and demonstrate intermediate level photometric calibration with FORS1.

As a first step, we have investigated the accuracy of relative photometry with FORS1 in the FSSWG project. The key results presented by Møller et al. (2005) was that the magnitude zero point varies by about 5 percent over the FORS1 image when standard master flats are used for flatfielding. That report also proposed a way to correct for such zero point variations. Subsequently, the *FORS Absolute Photometry Project (FAP)* was started to investigate the absolute accuracy of photometry with FORS1. The specific goal of *(FAP)* was to demonstrate the feasibility of 3 percent photometry, and describe procedures and give advice to both ESO and observers on how it can be reached. This report describes the methods, results and recommendations of *FAP*.

3 Relative Photometry with FORS1

The ESO archive contains a huge collection of data which can be used to assess the current accuracy of photometry with FORS1. Before describing the new data collected for *FAP*, we discuss in this section two issues which might limit the accuracy of photometry which can be achieved with FORS1. The first is the effect of cosmic ray hits, and the second is the properties of twilight flats routinely collected for FORS1.

3.1 Effect of Cosmic Ray hits on FORS1 photometry

In order to evaluate the impact of cosmic ray (hereafter CR) hits on FORS1 photometry, we have investigated the CR rate of the FORS1 detector. The data used was a set of 5 dark frames of 1800 sec each taken on March 17, 2005. We identified CR hits as groups of adjacent pixels with intensities above a given threshold. The background level of each exposure was estimated as the median of all pixels, and the rms deviation σ was estimated using the Median Absolute Deviation (MAD). For Gaussian noise, MAD is related to the standard deviation σ as $\sigma = 1.48\ MAD$. The

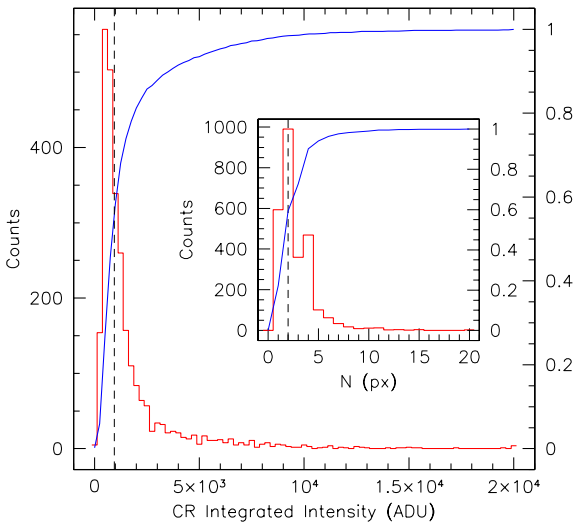

Figure 1: Example of CR integrated intensity distribution (red) and cumulative function (blue) measured on a FORS1 dark frame. The insert shows the corresponding distribution of number of pixels per CR event. In both plots the vertical dashed line marks the median of the distribution.

advantage of using MAD is that it is robust and avoids overestimation of noise due to the presence of CR. The derived values σ ≈6.2 e^- are very close to the nominal value of the read-out noise. Subsequently, all pixels with fluxes more than $k\sigma$ above the background were considered as affected by CR hits. Among them, groups of adjacent pixels were then counted as a single CR event and their integrated intensity was computed.

The resulting CR rate as a function of flux counts is shown in Fig. 1 for k=10. The CR rate, averaged over the 5 frames is 1.46±0.04 events/sec/frame, and the median integrated intensity is 970±30 ADU, while the median number of affected pixels per CR event is 2.

For the 10 sec exposures used in *FAP*, the expected number of CR hits is therefore about 15 which affect about 30 pixels. For a typical situation with about 200 detectable stars on the frame and a seeing is 1 arcsec (FWHM), on average less than one object will be affected by a CR within a 10 sec exposure. Therefore, for the purposes discussed in this report, the effects of CR can be safely neglected.

3.2 Twilight sky flat-field quality in FORS1

One of the most important ingredients to accurate field photometry is the flatfield correction. One area of concern for flatfielding are large scale features which are present in the flatfield but do not correspond to variations in the sensitivity as a function of position on the detector. If for example illumination gradients are present in the adopted flats, they are propagated into the science images and the resulting photometry will be affected by position dependent systematic errors.

Gradients in flatfields are often introduced by the illumination source, which is in the case of the FORS flats the twilight sky. In addition, gradients or other flatfield features can be introduced by the instrument, e.g. through scattered light. Both issues are discussed in this section.

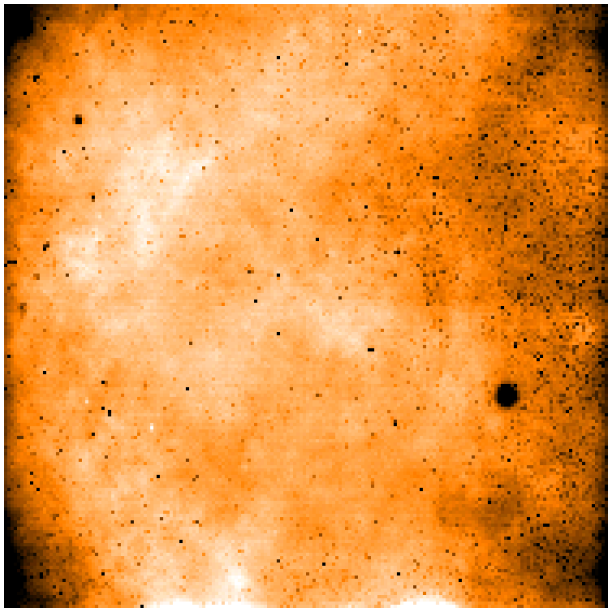

Figure 2: Example of raw twilight sky flat in the R passband. For presentation, the 4-ports pattern has been removed dividing each port by its nominal read-out gain. The intensity scale range is 3 percent. To increase the signal-to-noise, the original image has been binned in boxes of 11×11 pixels.

3.2.1 Twilight sky gradients

In the current implementation of the FORS calibration plan, $UBVRI$ twilight sky flats are obtained at the start and end of every night, usually in groups of 4 frames each. During twilight, the sky is known to show illumination gradients, which change with time and the position of the Sun relative to the pointing of the telescope. Under the conditions which are typical for FORS sky flats, the measured gradients can range from 2 to 5 percent per degree (Chromey & Hasselbacher, 1996). Given the field of view (FOV) of FORS ($6'.8 \times 6'.8$), this translates into natural gradients that range from 0.2 to 0.5 percent. On these small spatial scales, the illumination pattern is expected to be well approximated by an inclined plane, whose maximum gradient direction and intensity changes with the position of the Sun relative to the imaged sky. Intrinsic sky gradients should be removed from individual flats before stacking the images (as suggested by Chromey & Hasselbacher, 1996).

Observed FORS1 flats show structures which reach peak-to-peak values of more than 3 percent, i.e. an order of magnitude higher that typical twilight sky gradients. An example is shown in Fig. 2. A number of different structures with different spatial scales are visible. These structures dominate over the natural twilight sky gradients.

3.2.2 Instrumental features

In order to investigate in more detail the structure and amplitude of FORS1 intrinsic flat field features, we have downloaded from the ESO Archive all twilight sky-flats obtained between January 1, 2005 and September 30, 2005 in the $UBVRI$ passbands (Standard Resolution Collimator, 4-port read-out, high gain). The total number of images for all filters is 1083 (U: 148, B: 208, V: 226, R: 261, I: 240).

To speed up the reduction procedure, each individual frame has been bias-corrected using the

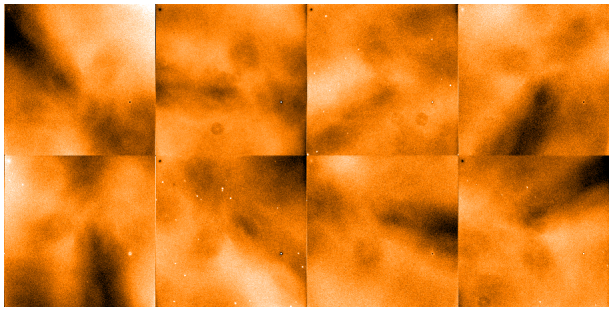

Figure 3: A sequence of B FORS1 sky-flats. The rotator adapter angle grows from upper left to lower right frames (-185, -145, -105, -73, -35, 0, $+30$, $+70$ degrees).

pre-scan region only. To remove the 4-port pattern and to eliminate the relative frame-to-frame variations, we have then computed for each filter a master flat stacking all available images, and used this master flat to correct all input frames. Finally, to allow a quick visual inspection, we have produced movies where each frame is a individual sky flat. From the inspection of these movies, we found that the structure in the flatfields seems to consist of a constant pattern superimposed on large scale fluctuations rapidly changing with time. The constant pattern appears to be more clearly visible in the blue bands and, most important of all, to rotate rigidly with the rotator adapter as shown in Fig. 3. This clearly indicates that whatever the cause of this structure is, it is external to FORS1 and might be due to reflections and/or asymmetric vignetting within the telescope or the adapter itself.

In order to produce a much higher signal-to-noise image of this pattern, we have counter-rotated all B images by an amount equal to the rotator angle reported in their FITS header and combined them with a median stacking. The result is shown in Fig. 4. The peak-to-peak amplitude of the pattern is about 1 percent. Inspection of individual images in the stack shows that the amplitude can be significantly higher or lower in some of the images.

The existence of this pattern poses a serious limitation on the maximum accuracy reachable with FORS. If the feature is due to a rotation of the sensitivity pattern imprinted on all science frames, one would need to carefully match the rotator angle of the flat to those of the science frame. If, however, this feature is an additive component to the flat, subtracting it from the flat would improve the photometric accuracy of all flatfielded science data. A possible procedure to remove the feature from sky flats would be to combine a large number of images taken with different rotator angles which should on average smooth out any rotating feature. As a test, we have applied this procedure to our R data set. From the global sample we have removed a suitable number of frames in order to get a roughly constant rotator angle distribution, so that there are no particular angles which are over-represented. Then we have computed a median stack, which is presented in Fig. 5. It can be seen that the resulting image appears to consist of a rotationally symmetric feature superimposed on an irregular pattern. A hint of a central light concentration is also visible, but it is quite shallow. This can be more easily seen in Fig. 6, where we plot cross-cuts along the central column and the central row.

Both features shown in Figs. 4 and 5 appear to be stable in time, at least on the scales explored by this investigation ($\sim$9 months). However, in addition to these stable features, there appears to be a component which varies in time.

This is illustrated in Fig. 7, where we compare two sky flats obtained about 12 hours apart. A clear change in the large saddle-shaped background is evident. This difference in the two flats is similar to a 90 degree rotation, even though the adapter rotator angle changed only by about 25

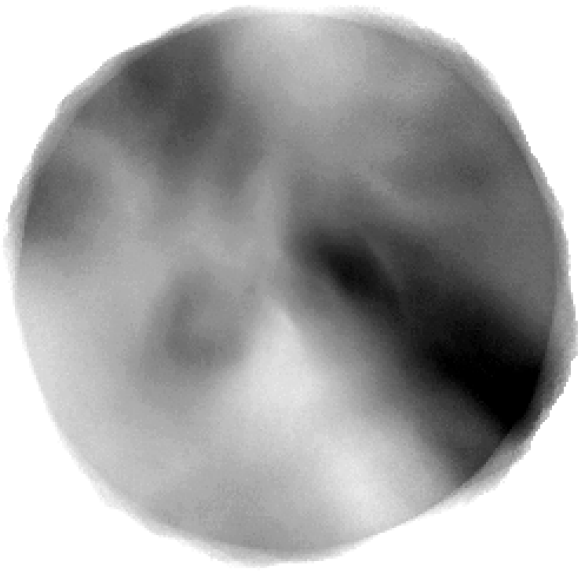

Figure 4: A stack of all B sky flats after applying a rotation around the geometrical centre with an amplitude equal to the adapter rotator angle reported in the FITS header of each input image. The intensity scale range is 1 percent.

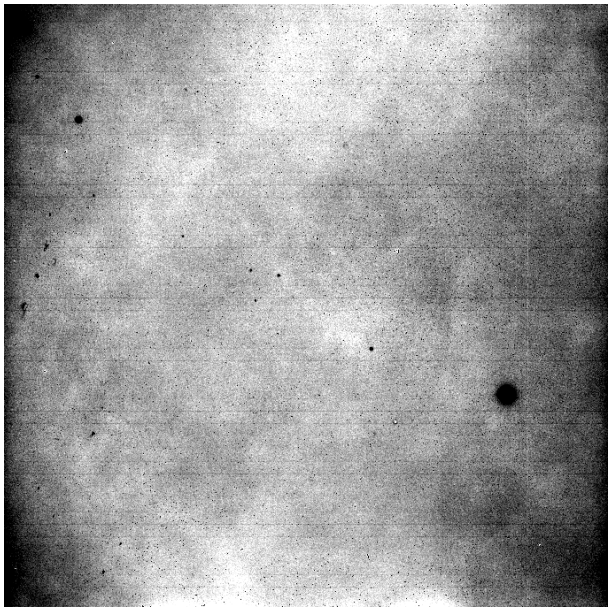

Figure 5: A stack of a selected sample of 240 R sky flats. For presentation, the 4-port pattern has been removed. The intensity scale range is 3 percent.

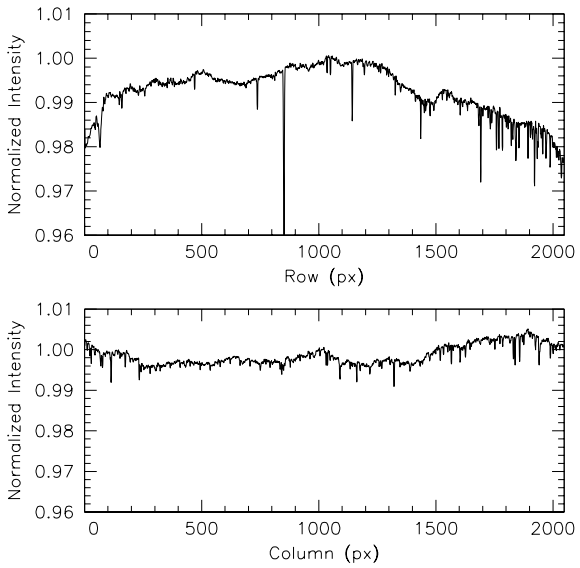

Figure 6: Traces along the central column (upper panel) and central row (lower panel) for the stack frame shown in Fig. 5. For presentation the traces have been normalised to their value at pixel 1024.

degrees. We also notice that large scale gradients are absent in some flats, as in the case shown in Fig. 2. The reason for such abrupt changes remains unknown.

3.2.3 Summary

The key finding of this section is that relative gradients in individual twilight flats as routinely obtained differ from each other by as much as 5 percent. If such flatfields are applied to science data, the relative photometric accuracy is limited to about 5 percent. Even when controlled for rotator angle, flatfields differ from each other by an amount which questions the goal of the current project, i.e. relative photometric accuracy of less than 3 percent. A key question is whether these fluctuations reflect true differences in the end-to-end throughput of FORS1. In that case, relative and therefore absolute accuracy at the percent level simply cannot be obtained with FORS. An alternative explanation is that the flatfields are flawed and do not represent the throughput of FORS1. In that case, the task is to find the true flatfield which should be applied to data so that photometric zero points are constant over the whole detector. In the following sections, we will use data from the *FAP* programme to test the quality of the flatfields constructed in this section, and compare it to the regular "master flats" produced by combining the routinely taken twilight flats for that night.

4 FAP Data

4.1 Observations

Obtaining 3 percent photometric accuracy requires: 1) relative photometric calibration within each field; 2) absolute calibration of the extinction relation with slope and zero point; and 3) calibration

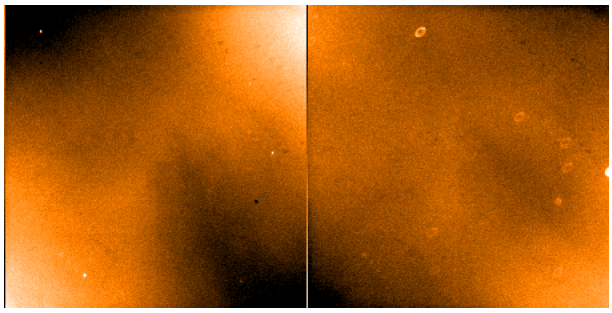

Figure 7: Comparison between two R flats taken on July 14, 2005 on 10:59:19.530 (left) and 22:43:32.037 (right). Both frames have been divided by the same master sky flat. The adapter rotator angle is -29.8 and -4.9 in the two images respectively. The intensity scale range is 3 percent.

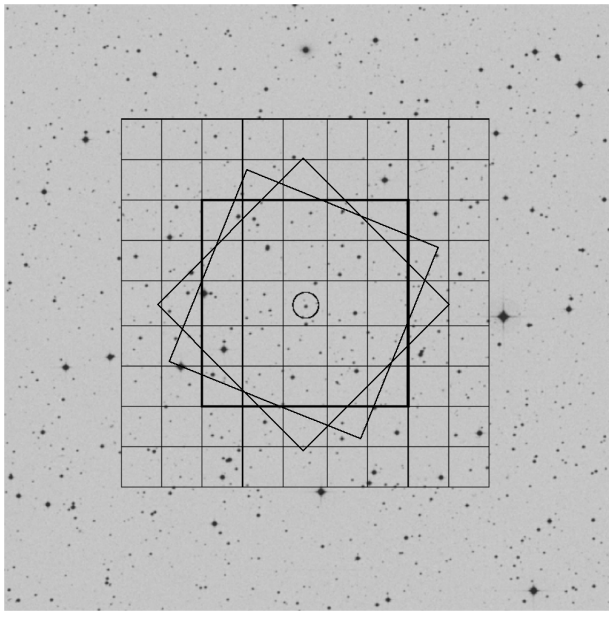

Figure 8: Pointings on the Stetson Mark A field. The outline of the FORS1 frames are shown superimposed on the DSS field of that region. The well observed standard star Mark A-S873, which is included in all frames is marked with a circle. Note the three different rotator angles used for the central field.

of colour terms. Methods and data to obtain accurate relative photometry within the FORS1 field have been presented by Møller et al. in report II of the FSSWG project (Møller et al., 2005, hereafter FWII). For the current project, we aimed at an independent assessment of the relative photometric calibration to investigate whether the FWII results can be reproduced.

Our observations consisted of a 5×5 grid of positions on the Stetson standard field Mark A (Stetson, 2000) observed at low airmass. In addition, we observed one pointing on the grid of positions with two extra position angles. The pointings are shown in Fig. 8. All observations of that field were obtained at airmasses between 1 and 1.2.

In addition, we obtained data for the three standard fields L92, L113 and PG1633 observed at airmasses between 1.1 and 2.9. The FORS FOV is much smaller than the Stetson fields. We selected subregions of the standard fields which avoided bright stars. Unfortunately, for L113 a bright star was included in the observed field by mistake. This star saturated the CCD and led to bleeding, high background and bias offsets. For that reason, only a small fraction of the stars on the L113 field were useful, and 4 images had to be completely discarded.

All observations were carried out in a single photometric night on July 17, 2005.

4.2 Basic Data Reduction

Standard subtraction of overscan region and bias frames were performed using the IRAF "xccdred" package.

In order to compare the quality of flatfields, we used three different flatfields and applied them to the full set of data. They are:

MASTER FLAT: Most reductions of FORS data use the "master flat" as produced by the FORS1 pipeline. This flat is basically the mean of the flats taken for the night of observations. Below we simply refer to this flat as "master flat".

ILLUMINATION-CORRECTED FLAT: As shown in the previous section, the large scale illumination of the flats is not stable and changes from exposure to exposure. We have therefore applied an illumination correction to the master flat by removing its large scale variation. We used the IRAF task "mkillumcor" for that purpose. This task heavily smooths the master flat and then subtracts this smooth version from the original master flat. The smoothing kernel used by mkillumcor is a boxcar function with fixed size in the central part of the image, and reduced size close to the edges. The minimum box size we used was 15 pixels, and the maximum 200 pixels. A 2.5σ clipping was used to exclude deviant points from the computation of the smoothed image.

ROTATION-CORRECTED FLAT: Finally, as an experiment, we also used the mean of the archive flats shown in Fig. 5. As described in section 3.2.2, the input flats were selected so that flats taken at any rotator angle are equally represented. Specifically, we removed flats until in each rotator angle bin of 10 degrees, the same number of flats were included. We will refer to this flat as the "rotation angle corrected flat".

4.3 Measurement of Magnitudes

Stars were identified and instrumental magnitudes were measured using Sextractor. Based on the inspection of the growth curve, we computed aperture magnitudes with an aperture radius of 2 arcsec, and compared them with Sextractor's "automag". The difference between the two

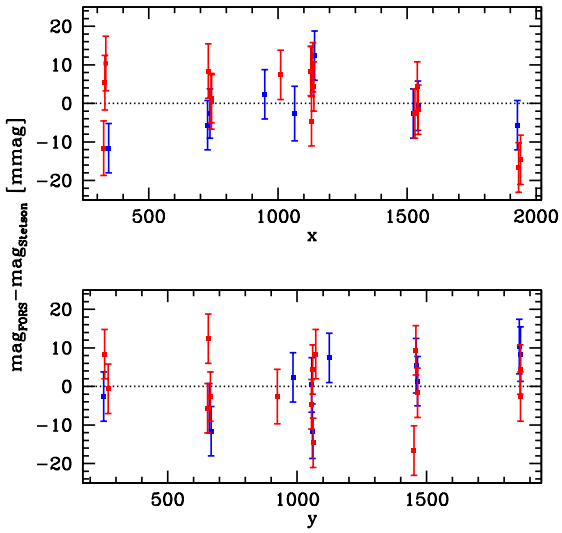

Figure 9: Relative instrumental magnitude of Mark A-S873 as a function of position on the CCD. In the upper panel, the y-coordinate of the star in each observation are colour coded. For $y > 1024$, point are red, and for $y < 1024$, points are blue. Similarly, in the lower panel the x-coordinate is colour coded, red for $x > 1024$, and blue for $x < 1024$.

magnitudes was found to be independent of the magnitude of the stars. Because of its smaller statistical error, the analysis was done using the "automag".

5 Zero point Variation across the FORS1 detector

The doubt about the quality of the flatfields discussed in Sec. 3.2.1 and raised by the FWII report warrants taking a closer look at any variations of the magnitude zero point across the detector when using the master flat. The goal is to derive a correction to the used flatfield similar to the one proposed by FWII to improve the accuracy of the flatfields. In addition, we aim to find a quantitative estimate of the accuracy of the final adopted flatfield.

5.1 25 Points of Light

The dithered observations were planned with the specific intent of placing one of the Stetson standard stars, namely Mark A-S873, on a grid of positions on the CCD (see Fig. 8). This approach is often nicknamed the "1000 points of light" approach, but we call it more modestly the "25 points of light". The simplest and most direct way to investigate relative zero point changes with such data is to plot the relative instrumental magnitudes of Mark A-S873 as a function of position. Such a plot is shown in Fig. 9. It can be seen that any relative photometric errors within the part of the detector sampled by our grid are on the order of 30 mmag or less. The sensitivity achieved with this analysis is insufficient to convincingly detect flat field variations.

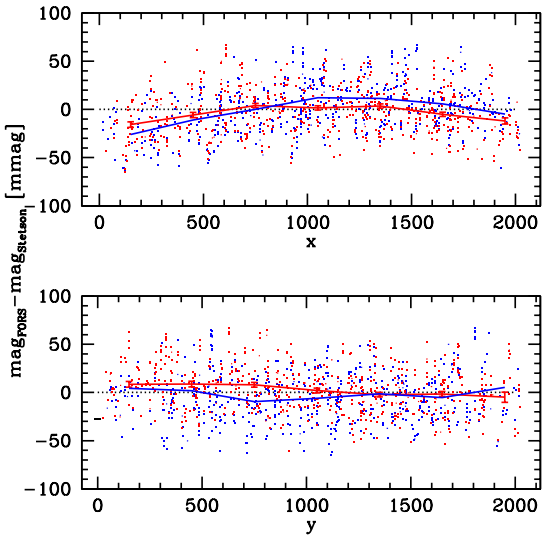

Figure 10: Relative instrumental magnitudes of stars in Stetson field Mark A as a function of position on the CCD. The colour coding is the same as in Fig. 9

5.2 1000 Points of Light

Better statistics than in Fig. 9 can be obtained by including all stars with magnitudes listed by Stetson. About 1000 magnitudes of Stetson stars have been measured from our data set. Fig. 10 plots the difference between instrumental magnitudes and Stetson magnitudes as a function of position on the detector. No bandpass correction was applied. The scatter for individual points in this plot is larger than the scatter in Fig. 9 because of errors in the Stetson magnitudes and because differences between the FORS1 and Stetson's effective filter shapes makes the zero point of stars depend on colour. This is more than compensated by the larger number of measurements. This larger data set clearly detects some deficiencies in the flatfield with total peak-to-peak error in relative photometry, within the inner part of the detectors of about 30 mmag.

5.3 Many Points of Light

5.3.1 Flatfield Correction Factor $f(x, y)$

The images of our data set contain many more stars suitable for photometry than the ones listed by Stetson. The large number of stars allows to simultaneously fit for relative zero points of each image, each star and zero point variations across the field. FWII describes a method to use measured magnitudes on a set of dithered images to simultaneously solve for relative zero point variations as a function of position on the detector, the relative magnitude zero point of each star and the relative magnitude zero point of each field. The power of this approach comes from the much larger number of stars which can be used to improve the statistics compared to the previous approaches. By contrast, the number of free parameters (one for each star and observed field) increases only modestly.

FWII defined a flatfield correction factor $f(x, y)$, so that each measured magnitude of a star on

any of the images can be written as

$$m_{\nu\mu} = M_\nu + z_\mu - f(x, y) \tag{1}$$

where M_ν is the magnitude of star ν within the chosen band, $m_{\nu\mu}$ is its instrumental magnitude measured on image μ, and z_μ is the zero point of image μ. Following FWII's approach, we used a polynomial to model $f(x, y)$,

$$f(x, y) = \sum_{i=0}^{o} \sum_{j=0}^{o-i} p_{ij} x^i y^j. \tag{2}$$

The formalism to compute $f(x, y)$ is described in Appendix A.

To estimate the uncertainties in the correction frame, we have carried out Monte-Carlo simulations in the following manner. First, we added normally distributed random errors to the measured magnitudes of each star. The standard deviation of the Gaussian was chosen to be identical to the error estimate in the actual measured magnitude. We created a total of 100 artificial data sets in this manner, and fitted $f(x, y)$ for each of them. We then computed the rms from all artificial data sets for each pixel.

5.3.2 Results

The resulting $f(x, y)$ flatfield correction is shown in Fig. 11. The peak-to-peak flatfielding error at the position of the observed stars is about 30 mmag. The peak-to-peak flatfield correction over the whole field is about 50 mmag. However, over a large fraction of the detector, the corrections are smaller than 10 mmag and the rms over the whole frame excluding a strip 200 pixels wide along the edge is only about $4\,mmag$. Therefore, while flatfielding problems on FORS1 might result in errors larger than our stated goal of 3 percent photometry for individual stars, statistically for random positions on the detector, the errors are much smaller. A different strategy for achieving accurate relative photometry with FORS is to concentrate on the centre part of the detector. For example, within the central 4×4 arcmin of the detector, roughly one third of the detector area, the difference between the minimum and the maximum of the correction factor is about 13 mmag, and the rms is 2 mmag.

5.3.3 Comparison with FSSWG

The FSSWG project used a similar procedure to the one used for the current work. In Fig. 12 and 13, we compare the results of the fit to the one in FWII. It can be seen that there is a good correlation between the two flatfield correction frames from data taken more than a year apart. The differences between the two determinations of $f(x, y)$ are similar in magnitude to the error estimates in $f(x, y)$. This suggest that there is a stable flatfield correction which can be applied to improve the photometric quality of images taken with FORS1 in the R-band.

6 Improving the Master Flat

In section 3.2.2 we have shown that a substantial component of the structure in the master flatfield rotates with the rotator. It is unlikely that any feature in the sensitivity map, i.e. the "true" flat field, rotates. Therefore, it is most likely that the rotating feature is a defect in the master

Figure 11: R-band flatfield correction frame.

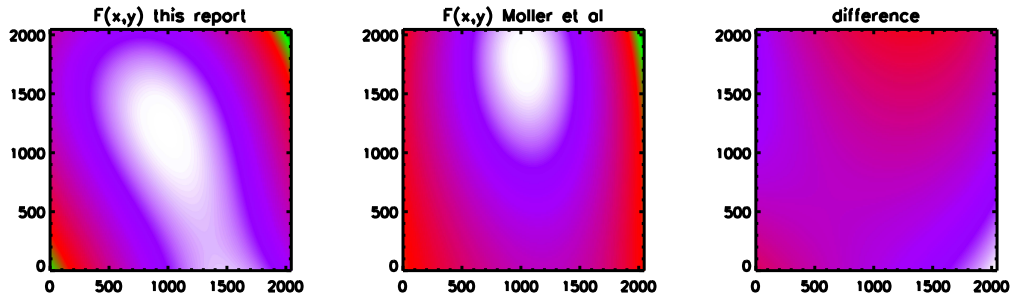

Figure 12: Comparison between the flatfield correction frames derived in the current work and FWII. The left panel shows $f(x, y)$ from *FAP*, the centre panel the one from FWII, and the right panel the difference. The colour scale in all three panels is identical.

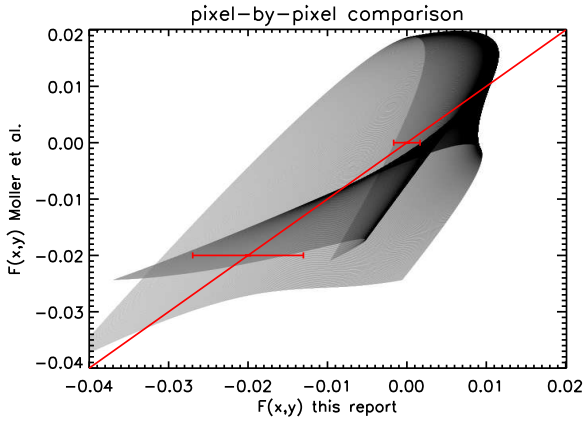

Figure 13: Pixel-by-pixel comparison of $f(x, y)$ found by FWII and in the current project. The gray level indicates the number of pixels with the corresponding combination of values found by the two fits. The red line illustrates a one-to-one correspondence of the plotted values. The error bars are the minimum and maximum rms uncertainty for $f(x, y)$ estimated from the Monte-Carlo simulations. The differences between the two frames are comparable to the uncertainty in the fits.

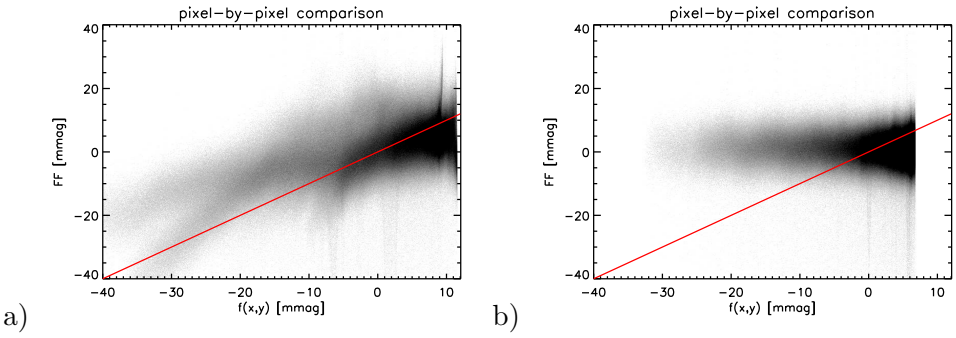

Figure 14: Pixel-by-pixel comparisons of $f(x, y)$ with the flatfield (FF) used to process the images before fitting $f(x, y)$. Panel a) shows the case of the master flat, and panel b) the case of the illumination-corrected flat.

flats, e.g. caused by light scattered on some structure connected with the rotator. In this case, the derived flat field correction should compensate for some of the structure found in the master flat. In panel (a) of Fig. 14, we compare the master flat with the derived $f(x, y)$ on a pixel-to-pixel basis. We find that there is a significant correlation between the two frames. This suggests that the master flat could be improved simply by removing its large scale pattern.

This motivated us to create the illumination-corrected flat described in Sec. 4.2. We used the images flatfielded with this modified flat to re-measure magnitudes and re-derive the flatfield correction factor. A pixel-by-pixel comparison of the illumination-corrected master flat with the re-derived correction factor is shown in panel b of Fig. 14. It can be seen that any correlation between flat and correction factor has successfully been removed, and that the peak-to-peak values of the correction factor have become smaller. This demonstrates that the master flat can be improved simply by this simple procedure. We also tested the same procedure on the I-band data, and on the FWII data and found similar results.

The standard stars on the images can be used to verify that the flatfielding is indeed improved by this procedure. For that purpose, we have derived photometric solutions from the standard star measurements as described in section 7 but without using the flatfield correction factor $f(x, y)$. The residuals as a function of detector position for the case of the regular master flat and that of the illumination-corrected flat are compared in Fig. 15. It can be seen that the illumination correction improves by as much as 50 percent of the error in the centre of the field. However, it also shows that even using the illumination-corrected flats, significant flatfielding errors remain and the flat field correction procedure is still needed to reduce residual flatfield errors to values below 1 percent.

We have also tried the same procedure using the rotation-corrected flat shown in Fig. 5 but found no improvement over the standard master flat. We therefore will not use that flat in the further analysis.

7 Absolute Photometry

7.1 Photometric Quality of Night

A crucial requirement for *FAP* was that observations were carried out under photometric conditions. The judgement whether a night is photometric is done by the weather officer. This judgement is based on zeropoints provided by imaging instruments and inspection of the sky with MASCOT and by eye. If a science programme demands photometric quality and observations are carried out in service mode, it is essential that the observer can judge the quality of the night objectively. For *FAP*, the photometric quality of the night can be judged from the collected data. This might not be the case for science observations if significantly fewer calibration observations are taken during the night.

A useful tool to judge the quality of the night might be the "VLT Astronomical Site Monitor" (ASM). Figure 16 shows the ASM flux fluctuations during the the course of the night. All images were taken after UT 2:20 when the rms of the fluctuations was less that 10 mmag. The mean rms fluctuation during the course of the observations was about 7 mmag. These data can be compared to the flux fluctuations derived from the observations.

A side product of the solution of for the flatfield correction in the previous section is the relative zero point shift for each field. The relative zero points of the Mark A field are based on the weighted average of more than 1000 stars on each of the images and the statistical error for them are on the order of one mmag. They are almost independent of flatfielding errors. Changes in the relative

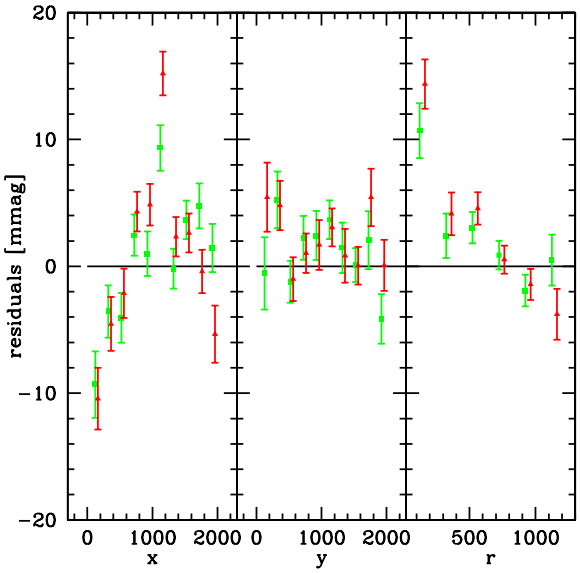

Figure 15: Residuals from fit of photometric solution as a function of detector position. The left, centre and right panels show the mean residuals as a function of column x, row y and distance from the detector centre r. The red points are derived using the regular master flat, and the green points used the illumination-corrected master flat. No flatfield correction $f(x, y)$ has been applied. Error bars are the errors of the means based on error estimates for the measured magnitudes and listed errors of the standard stars. Note that the mean of all the residuals is by construction zero. In the left most panel, the inner point contains fewer stars because it is based on a small area on the detector.

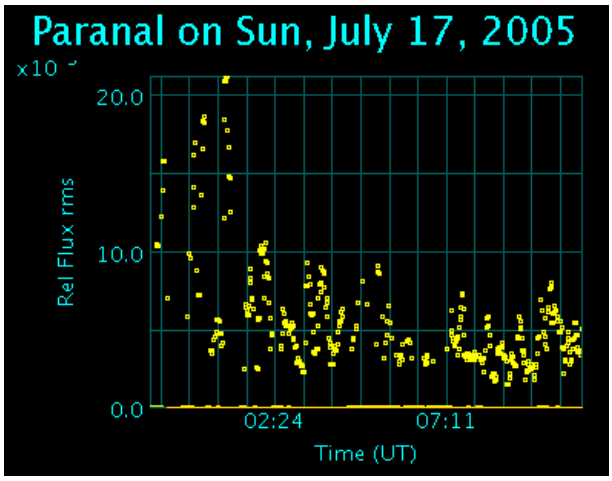

Figure 16: The rms flux as measured by the ASM monitor.

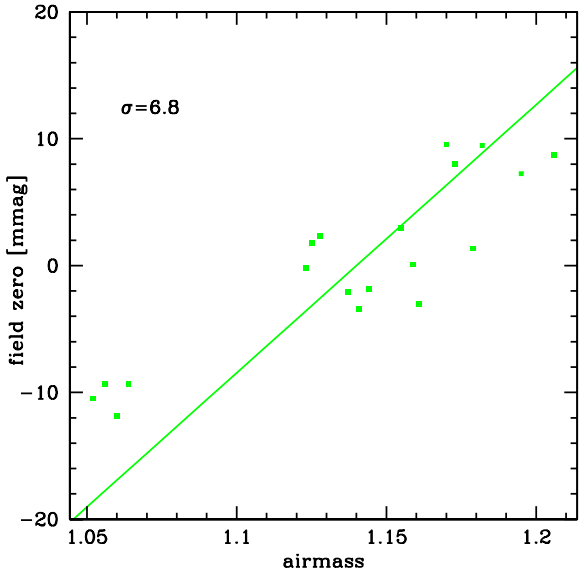

Figure 17: Relative zero points of individual exposures of the Mark A field as a function of airmass as determined from the simultaneous fit of $f(x, y)$, relative magnitudes of stars and the exposure zero points. No standard magnitudes were used in deriving these data points. The solid line is the slope of the extinction correction as determined from the fit to Stetson magnitudes of stars. The rms of the deviations from this line is 6.8 mmag.

zero points are therefore a highly accurate measure of changes in the extinction between different images.

Figure 17 shows the relative magnitude zero points for the Mark A images as a function of airmass. The error estimate for each of the points based on the measurement errors is smaller than the point size. Also shown is the slope of the extinction curve derived from fields taken at higher airmasses, the details of this determination will be discussed in section 7.3. It can be seen that the slope of the extinction curve is in excellent agreement with the variations of the zero point as a function of airmass. The rms scatter of the zero points around the extinction curve is 6.8 mmag. This experiment confirms the excellent photometric quality of the night completely independent of any standard star magnitudes.

The scatter of 6.8 mmag is a good measure of the fluctuations in the extinction within the 10 sec exposures. Its value is similar to the flux rms measured by the ASM monitor. It is tempting to conclude that the rms from the ASM can be used as a proxy for expected rms fluctuations of the zero point. Whether this is indeed the case warrants further investigation. One area of concern is its sensitivity to seeing changes.

7.2 Photometric Solution

The method used to find the flatfielding correction can easily be modified to find a photometric solution from the current data set. Instead of using an arbitrary zero point for each star and each field, the photometric zero point, colour terms and extinction coefficients are fitted. Specifically, we assumed that the instrumental magnitudes r and the Stetson magnitudes R and I are related as

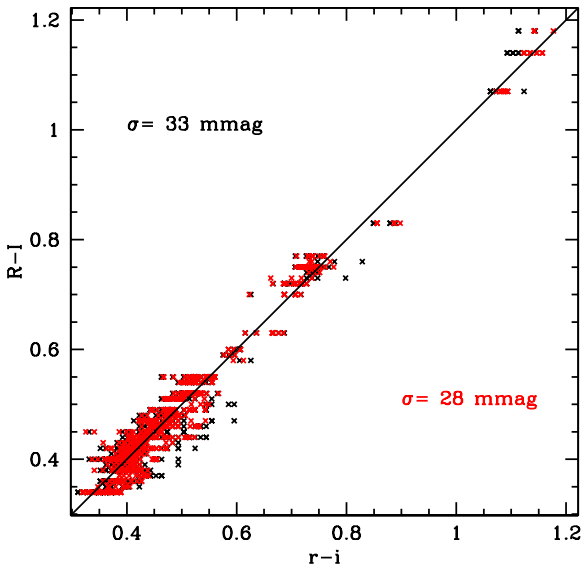

Figure 18: R-I colours listed by Stetson versus the colours computed from the *FAP* data. Points in black use the colours based only on a fit of the zero point and slope of the colour correction, whereas red points use the full airmass and quadratic terms.

$$R - r = z + e \cdot x + a \cdot (R - I) + c \cdot (R - I) \cdot x \tag{3}$$

where x is the airmass and z, e, a and c are parameters determined by the fitting. Those parameters were fitted simultaneously with the flat fielding correction. The formalism is described in Appendix B .

We compared this solution to a separate fit of the correction frame $f(x, y)$ followed by a fit of the photometric solution. We found no differences in the results. All results in this section are based on the illumination-corrected flatfields and the additional application of the flat field correction derived from all detected stars.

Colour coefficients were fit using

$$r - i = c_z + c_e \cdot x + c_a \cdot (R - I) + c_c \cdot (R - I) \cdot x + c_d \cdot (R - I)^2 \tag{4}$$

The fit is shown in Fig. 18. The scatter in the predicted colours from the fit is about 28 mmag. The uncertainty in the true colour adds less than 3 mmag of scatter to the final R magnitude when measured colours are used in Equ. 3.

7.3 Results

7.3.1 Extinction Solution

The resulting extinction solution is shown in Fig. 19. The ESO Quality Control (QC) derives a photometric zero point assuming an extinction for each night. This QC zero point and extinction for that night are also shown in Fig. 19. There is a small offset between the normalisation of the QC extinction curve and the one derived here at airmass around 1.2. This offset might be

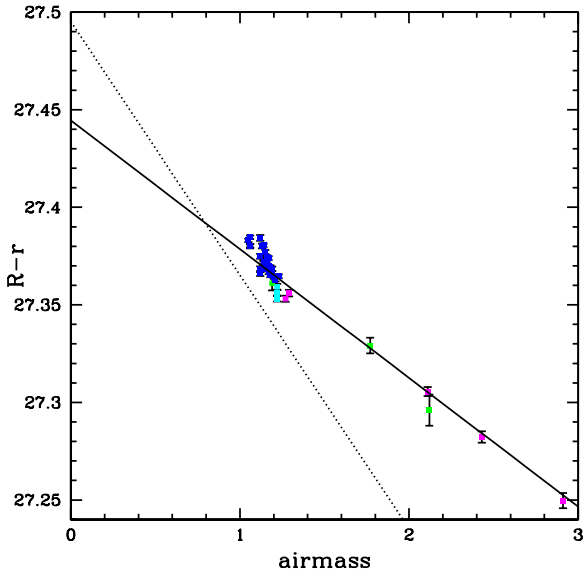

Figure 19: Extinction solution: R-r corrected for colour and colour-dependent extinction as a function of airmass. Each point is the weighted mean of all stars in one image. The colour of each point indicates the Stetson field from which the point was derived. The codes are: blue: Mark A, green: L 113, magenta: PG 1633 , cyan: L 92. The solid line is the fit to the data points and the extrapolation to zero airmass is shown to illustrate the magnitude zero point. For comparison, the photometric zero point and assumed extinction from the QC pipeline for that night is shown as a dotted line.

due to slight differences in the normalisation of the flatfields, differences in the apertures used to measure magnitudes, and/or differences in the colour coefficients. However, the assumed extinction in the QC procedure introduces an additional error in the zero point which is much larger than the differences at airmass around 1.2. The extinction varies substantially from night to night, even when the nights are photometric. Therefore, zero points derived using a mean extinction depend on the airmass of the measured standard field and are not useful for photometry. The true photometric zero point above the atmosphere as derived from extrapolation of the extinction curves probably varied much more slowly than the night-to-night variations of the extinction. For this reason, when only a single photometric standard observation is available in a given night, the best practise is to derive the extinction coefficient for that night by assuming the zero point has not changed from the previous determination (cf. e.g. Harris, 1981).

7.3.2 Residuals and Error Budget

Sextractor computes error estimates σ_s for each measured magnitude. The error includes the contribution of the readout noise and Poisson noise, both for the pixels used to compute the stellar flux and for those used to estimate the local background. The error estimates ranged from 2 to 30 mmag. Stetson (2000) and Stetson (2006) list error estimates σ_{st} for individual standard stars based on repeated observations in different nights. The error estimates for the stars used in this analysis range from 2 to 20 mmag. By comparing these error estimates to the residuals of the extinction solution, we can find an external estimate of the combined effect of *all sources of errors* not included in σ_s and σ_{st}. For this purpose, we plot the residuals from the extinction solution as a function of the error estimate σ_M for each $R-r$. The plot is shown in the upper panel of Fig. 20. The error estimate σ_M was computed as $\sigma_M = \sqrt{\sigma_s^2 + \sigma_{st}^2}$. It can be seen that the scatter in the residuals for small estimated errors is less than 10 mmag and increases for larger σ_M. The lower panel of Fig. 20 shows the rms of the residuals binned by error estimates. A source of scatter in addition to the error estimate has to be assumed to account for the scatter residuals. If this additional scatter σ_a is independent of magnitude, then the total scatter in the residuals $\sqrt{\mathrm{VAR}}$ can be modelled as

$$\mathrm{VAR}^2 = \sigma_s^2 + \sigma_{st}^2 + \sigma_a^2 \tag{5}$$

The lower panel of Fig. 20 shows that a value of $\sigma_a \approx 7$ mmag is consistent with the residuals.

Sources for σ_a include extinction fluctuations σ_e, colour transformation errors σ_c and residual flatfielding errors σ_{ff}. The total error estimate σ_t for our magnitude measurements becomes therefore

$$\sigma_t = \sqrt{\sigma_s^2 + \sigma_a^2} = \sqrt{\sigma_s^2 + \sigma_e^2 + \sigma_c^2 + \sigma_{ff}^2} \tag{6}$$

In Sec. 7.1 we found that $\sigma_e \approx 7$ mmag, and in Sec. 7.2 we estimated that $\sigma_c \approx 3$ mmag. Using 8 mmag as the upper limit for σ_a, we find from Equ. 6 an upper limit on residual flatfielding and other sources of errors of about 3 mmag. We therefore conclude that extinction variations, statistical errors and errors in the standard magnitudes account for most of the residuals of our photometric solution.

7.4 How many Standard Field Observations are necessary?

An important goal of this project is to find a set of guidelines on how to achieve a photometric accuracy of 3 percent or less. The photometric zero point is obviously an important factor which

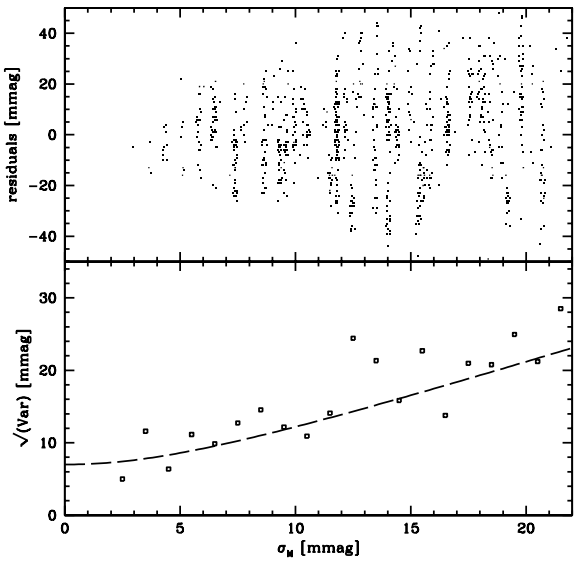

Figure 20: Upper panels: Residuals as function of the estimated magnitude error. Lower panel: The $\sqrt{\text{Var}}$ of the residuals as a function of magnitude error. The superimposed line corresponds to Var= $(7\text{mmag})^2 + \sigma_M^2$.

determines the final accuracy of the magnitudes. The *FAP* observations contain a large number of standard stars on each individual image, and the number of calibration images is much bigger than the number realistically taken for the calibration of normal science observations. An important part of the photometric guidelines are the necessary minimum number of standard fields needed to achieve certain science goals.

FAP imaged four different Stetson fields. The magnitude and colour range, and the consistency of derived zero points seems to be similar for all fields (see e.g. Figs. 19). In addition, we searched for and did not find any evidence for different behaviour of the residuals as a function of position, magnitude or colour. Therefore, there is no evidence than anyone of the three fields Mark A, L92 or PG1633 is better suited for photometry than any other. As discussed in Sec 4.1, the particular region we used within the L113 field was not optimally chosen. Excluding the L133 field from the analysis in this section did not change any of the conclusions. For that reason, we do not distinguish between the different fields in the following discussion.

If a night is known to be photometric, a minimum of 2 calibration fields at different airmasses are needed to find the extinction coefficient. The optimum strategy is that one of them is at as low an airmass as possible, while the other one is at the highest possible airmass. A realistic goal is to observe the low airmass field at an airmass less than 1.3, and the high airmass field at airmass above 2.

To estimate the errors in the zero points from sets of only two standard field observations, we re-computed the zero points from subsets of the *FAP* data. We used every combination of two standard fields which satisfy the above constraints on the airmasses. The distribution of the resulting zero points is shown in Fig. 21. The distribution has an almost Gaussian peak but also a long non-Gaussian tail. In about 10 percent of all cases, the errors on the resulting zero points is larger than 3 percent. We therefore conclude that observation of only two standard fields is insufficient to photometrically calibrate a night to sufficient accuracy.

We then repeated the experiment using 3 standard fields. In each case, only one of the three fields was chosen to be at airmass lower than 1.3, because the gain from additional low airmass fields was judged to be small. The resulting distribution of zero points is plotted in Fig. 21. Also shown is a Gaussian with the same mean, standard deviation and normalisation as the zero point distribution. It can be seen that the distribution resembles closely a Gaussian with a standard deviation of 11 mmag. In contrast to the previous experiment with only two standard fields, all zero point errors are less than 3 percent. This result strongly suggests that 3 photometric standard fields, chosen with the strategy outlined above, lead to an accuracy of about 11 mmag.

The χ^2 per degree of freedom of the deviation between the Gaussian fit and the histogram in Fig. 21 based on count statistics is about 0.85. This means than the distribution of zero points when using 3 different standard fields very closely follows a Gaussian distribution. The error budget discussed in Sec. 7.3.2 implies that the dominant error on the mean magnitude of all stars in any of the standard fields are fluctuations in the extinction which affects all stars of an image in the same way. The only way to improve the magnitude zero point is therefore to increase the number of independent exposures. The fact that the distribution of the residuals shown in Fig. 21 is normal suggests that adding more stars will improve the accuracy of the zero point, and the final error in the zero point σ_Z is

$$\sigma_Z \approx 11\,\mathrm{mmag} \cdot \sqrt{\frac{3}{n_f}} \tag{7}$$

where n_f is the number of standard field observations. This formula should apply if the number of standard stars in each field is large enough so that

$$\sqrt{\frac{1}{\sum \frac{1}{\sigma^2_{\mathrm{STD}}}}} \ll 11\,\mathrm{mmag} \tag{8}$$

and the exposures sample the airmass between 1 and 2 uniformly. For a typical magnitude uncertainty σ_{STD} of 10 mmag, about 100 standard stars are needed to satisfy Equ. 8. Unfortunately, the *FAP* data do not include a sufficient number of independent observation to test formula 7 for n_f larger than 3.

The zero point error is a systematic additive error which affects all derived magnitudes in the same manner. The exact impact of such an error depends on the science application. In most cases, a programme with a stated goal to achieve 3 percent photometry requires that the systematic error is significantly less than 3 percent. The 10 mmag accuracy for the zero point might therefore not be sufficient for many photometric programmes even when they can accept much higher random errors. Equ. 7 can be used to guide observers. For example, the goal to achieve a photometric zero point better than 20 mmag with 99.7 percent confidence implies a 3σ error for the zero point of 20 mmag. Equ. 7 implies that eight standard fields are needed.

7.5 Three Percent Photometry

The above discussion shows that 3 percent photometry can be reached with FORS1 with moderate effort. For the purpose of this discussion, three percent photometry is defined as a total 1σ error including both random errors on individual star and systematic errors due to zero point. With three calibration fields, the error in the zero point is 11 mmag (Sec. 7.4). The maximum possible systematic error is 3 mmag (Sec. 7.3.2). This leaves $\sqrt{30\,\mathrm{mmag}^2 - 11\,\mathrm{mmag}^2 - 3\,\mathrm{mmag}^2} = 27.8\,\mathrm{mmag}$ for the possible random error in the magnitude of the science targets. A standard 1 hour OB results in 50 minutes of open shutter exposure time. Using the ESO Exposure Time Calculator, we find

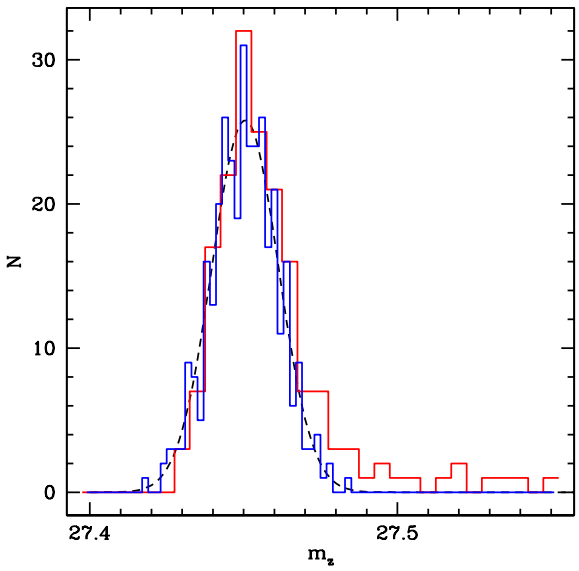

Figure 21: Distributions of zero points determined from two (red histogram) and three (blue histogram) standard observations. The dashed line is a Gaussian with a σ of 11 mmag.

that under standard conditions, the 3 percent goal can be reached down to a R band magnitude of 24.3.

8 Proposed Procedures

The main result of *FAP* is that it is possible to achieve 3 percent photometry with FORS1 with moderate effort. We propose several changes to currently used procedures which will improve the routine photometric calibration of FORS1, collect the data to further improve the calibration, and allow service mode observers to specify the desired photometric calibration level.

8.1 Nightly Procedure for Obtaining Photometric Standards

Based on the discussion in the previous sections, we propose the addition of a second photometric standard observation as part of the routine calibration for each photometric night, using the Stetson fields for the observations, and introduction of an offset between the pointings each night in order to accumulate data with a dither pattern similar to the one we analysed in *FAP*. The aim of this proposal is to collect the necessary data for deriving 2nd order flatfield corrections, photometric zero points and colour coefficients as well as nightly extinction corrections. The specific procedure to follow each night is the following.

1. Continue to take a standard field at the beginning of each night. The field should be selected from the list of Stetson fields. Select the field with the lowest possible airmass.

2. For each observation of a Stetson standard field, select a position different from the previous observation of the field with the same filter in such a manner, that at least a 3×3 grid of position plus at least 2 rotator angles are accumulated on every standard in the course of time. Subsequent observations of the same field should be used to fill in the full 5×5 point grid

used in *FAP*. For that purpose, it is necessary to make the records of previous observations available to the night assistant.

3. Depending on the availability of fields, take a second standard field either at the beginning or end of the night. The difference in the airmass between the standard field at the beginning of the night should be at least 1.

With these data, the photometric zero point can be determined for each night and changes in zero point can be monitored with much higher accuracy than with the current procedure. Furthermore, if the zero point is, as expected, stable over time periods of several weeks, computing its mean over such time frames will result in highly accurate determination of the zero point which can be used for photometric work.

8.2 Procedure for Requesting Photometric Calibration

Currently, the only way for service observers to request improved calibration is to write instructions into the README section of OBs. However, since it is not known to the observers when the science OBs will be executed, it is difficult to specify a good calibration strategy. At the same time, it is difficult for ESO to charge observers for the time used for implementing such instructions. A more systematic procedure would therefore both help the observers to state their requirements and ESO to charge observing programmes in a fair manner. We propose the following simple scheme for implementing photometric calibration requests in OBs.

1. A parameter n_{photcal} should be added to OBs which specifies the number of requested photometric standard calibration fields. During the night of observation of that OB, the night assistant will choose the standard fields and carry out the observations according to specified criteria.

   The criteria for selecting the standard field are as follows. The first field will be at an airmass of less than 1.3. The second field will be at an airmass of 2 or higher. Additional fields will be chosen at intermediate airmasses. As discussed above, the specific region within each Stetson field should change from night to night.

2. Observers will be charged a predefined amount of time for each requested photometric calibration observation. The amount is computed from the actual time it takes to execute a standard observation, multiplied by a factor larger than unity. This factor adjusts for the fact that a requested standard observation might trigger observations of standard fields in nights which later turn out to be non-photometric and which are therefore not used for the science observation. The exact value for the correction factor should be determined from experience, but it might initially be set to 1.5.

Alternatively, more specific instructions to observers how to structure and write the README file could be used if it is not feasible to change the OBs this way in the short term.

APPENDIX

A Formulae to fit $F(x, y)$ from stars without known magnitudes

In general, each measured magnitude on any of the images can be written as

$$m_{\nu\mu} = M_\nu + z_\mu - f(x, y) \tag{9}$$

where M_ν is the magnitude of star ν within the chosen band, $m_{\nu\mu}$ is its instrumental magnitude measured on image μ, and z_μ is the zero point of image μ. The quantity $f(x, y)$ is $F(x, y)$ expressed in magnitudes, i.e.

$$f(x, y) = -2.5 \log F(x, y) \tag{10}$$

The specific model for $f(x, y)$ used for the fit to the current data set is a polynomial of order o,

$$f(x, y) = \sum_{i=0}^{o} \sum_{0}^{i} p_{ij} x^i y^{o-i}. \tag{11}$$

The magnitude for the $n + 1$ different observed stars, M_ν where $\nu = 0 \ldots n$, and the zero points of the $m+1$ different images, z_μ, $\mu = 0 \ldots m$, are further free parameters. Two of the three parameters $p_{0,0}$, M_0 and z_0 are redundant and can be arbitrarily fixed. Choosing $M_0 = z_0 = 0$, the full set of equations 11 can be written as

$$\mathbf{A} \cdot \mathbf{p} = \mathbf{M} \tag{12}$$

where $\mathbf{p}$ is the parameter vector

$$\mathbf{p} = \begin{pmatrix} p_{0,0} \\ p_{1,0} \\ p_{0,1} \\ \vdots \\ p_{kl} \\ M_1 \\ M_2 \\ \vdots \\ M_n \\ z_1 \\ z_0 \\ \vdots \\ z_m \end{pmatrix} \tag{13}$$

M is the vector of measured instrumental magnitudes,

$$\mathbf{M} = \begin{pmatrix} m_{0,0} \\ m_{1,0} \\ m_{2,0} \\ \vdots \\ m_{n,0} \\ m_{0,1} \\ m_{1,1} \\ \vdots \\ m_{n,m} \end{pmatrix} \tag{14}$$

and the matrix **A** is

$$\mathbf{A} = \begin{array}{c} \\ 0 \\ 1 \\ 2 \\ \vdots \\ n \\ n+1 \\ n+2 \\ \vdots \\ n \times m \end{array} \begin{array}{c} \begin{array}{ccccccccccccc} p_{0,0} & p_{1,0} & p_{0,1} & \cdots & p_{kl} & M_1 & M_2 & \cdots & M_n & z_1 & z_2 & \cdots & z_m \end{array} \\ \begin{pmatrix} 1 & x_{0,0} & y_{0,0} & \cdots & x_{0,0}^k y_{0,0}^l & 0 & 0 & \cdots & 0 & 0 & 0 & \cdots & 0 \\ 1 & x_{1,0} & y_{1,0} & \cdots & x_{1,0}^k y_{1,0}^l & 1 & 0 & \cdots & 0 & 0 & 0 & \cdots & 0 \\ 1 & x_{2,0} & y_{2,0} & \cdots & x_{2,0}^k y_{2,0}^l & 0 & 1 & \cdots & 0 & 0 & 0 & \cdots & 0 \\ & \vdots & & & & \vdots & & & & & \vdots & & \\ 1 & x_{n,0} & y_{n,0} & \cdots & x_{n,1}^k y_{n,1}^l & 0 & 0 & \cdots & 1 & 0 & 0 & \cdots & 0 \\ 1 & x_{1,1} & y_{1,1} & \cdots & x_{1,1}^k y_{1,1}^l & 0 & 0 & \cdots & 0 & 1 & 0 & \cdots & 0 \\ 1 & x_{2,1} & y_{2,1} & \cdots & x_{2,1}^k y_{2,1}^l & 1 & 0 & \cdots & 0 & 1 & 0 & \cdots & 0 \\ & \vdots & & & & \vdots & & & & & \vdots & & \\ 1 & x_{n,m} & y_{n,m} & \cdots & x_{n,m}^k y_{n,m}^l & 0 & 0 & \cdots & 1 & 0 & 0 & \cdots & 1 \end{pmatrix} \end{array} \tag{15}$$

The parameters corresponding to each column are shown on the top of the matrix. Note that only a subset of all stars is contained in any single image, the labelling of the rows on the left side of the matrix is therefore not necessarily consecutive. The total number of free parameters to be determined n_p is

$$n_p = n + m + \sum_{i=0}^{o}(i+1) = n + m + \frac{o^2 + 3o + 2}{2} \tag{16}$$

whereas the number of equations is identical to the number of measured instrumental magnitudes. If the number of instrumental magnitudes per image is >> 2, then Equ. (12) is an over-determined set of linear equations.

Singular Value Decomposition (SVD) can be used to find the unknown zero points, magnitudes and model parameters simultaneously in a least-square sense. SVD works by decomposing the matrix **A** into a square diagonal matrix **w** with positive or zero elements, and two orthogonal matrices **u** and **v**,

$$\mathbf{A} = \mathbf{u} \cdot \mathbf{w} \cdot \mathbf{w^t}. \tag{17}$$

Then the least square solution for **M** can be found as

$$\mathbf{p} = \mathbf{v} \cdot \mathbf{w'} \cdot \mathbf{u^t} \cdot \mathbf{M} \tag{18}$$

where $\mathbf{w'}$ is a matrix which consists of a the inverse of a $n_p \times n_p$ submatrix of **w** and is set to zero elsewhere (see Press et al., 1992, for details).

One consideration for solving this set of equations is to assign proper weights to each equation. Equ. (12) still holds when each row in the matrix **A** as well as corresponding elements of the vector of instrumental magnitudes are multiplied by an arbitrary weight. We weighted each equation taking into account both the uncertainty in the measured instrumental magnitudes and the local density of stars.

The estimated uncertainty $\sigma_{\nu\mu}$ in the instrumental magnitude of the ν^{th} star in the μ^{th} field as given by Sextractor were used to compute a weight w_m,

$$w_m = \frac{1}{\sigma_{\nu\mu}^2} \tag{19}$$

A significant source of uncertainty in the fit of our model to the zero points is the difference between the true shape of $f(x, y)$ and that of the model polynomial. If an unweighted fit of a polynomial were used, more weight would be given to regions with high density of observed stars. This would introduce biases in the fit which can be avoided by adjusting the weights according to the local density of stars. Specifically, we have used the inverse of the local density of w_m to compute a second weight w_ρ,

$$w_\rho = \frac{1}{\sum w_m} \tag{20}$$

where the sum in this equation is taken over all magnitude measurements in cells of 128×128 pixels on the detector. The final weight used for each equation was

$$w_t = w_\rho \cdot w_m \tag{21}$$

B Formulae to fit $F(x, y)$ and extinction solution simultaneously

The formulae in Appendix A can easily be modified when the magnitudes of stars are known. The magnitude zero points for individual stars are replaced with the colour term, the zero points for individual images are replaced by the extinction terms, and the zero of the polynomial $p_{0,0}$ is replace by the constant magnitude zero point to find the parameters of Equ. 3.

The parameter vector **p** then becomes

$$\mathbf{p} = \begin{pmatrix} z \\ p_{1,0} \\ p_{0,1} \\ \vdots \\ p_{kl} \\ e \\ a \\ c \end{pmatrix} \tag{22}$$

M is in this case the vector of Stetson minus instrumental magnitudes,

$$\mathbf{M} = \begin{pmatrix} M_0 - m_{0,0} \\ M_1 - m_{1,0} \\ M_2 - m_{2,0} \\ \vdots \\ M_n - m_{n,0} \\ M_0 - m_{0,1} \\ M_1 - m_{1,1} \\ \vdots \\ M_n - m_{n,m} \end{pmatrix} \tag{23}$$

and the matrix **A** is

$$\mathbf{A} = \begin{array}{r} \\ 0 \\ 1 \\ 2 \\ \vdots \\ n \\ n+1 \\ n+2 \\ \vdots \\ n \times m \end{array} \begin{array}{c} \begin{array}{cccccccc} z & p_{1,0} & p_{0,1} & \cdots & p_{kl} & e & a & c \end{array} \\ \begin{pmatrix} 1 & x_{0,0} & y_{0,0} & \cdots & x_{0,0}^k y_{0,0}^l & X_0 & c_0 & X_0 \times c_0 \\ 1 & x_{1,0} & y_{1,0} & \cdots & x_{1,0}^k y_{1,0}^l & X_0 & c_1 & X_0 \times c_1 \\ 1 & x_{2,0} & y_{2,0} & \cdots & x_{2,0}^k y_{2,0}^l & X_0 & c_2 & X_0 \times c_2 \\ & \vdots & & & & \vdots & & \\ 1 & x_{n,0} & y_{n,0} & \cdots & x_{n,1}^k y_{n,1}^l & X_1 & c_n & X_1 \times c_n \\ 1 & x_{1,1} & y_{1,1} & \cdots & x_{1,1}^k y_{1,1}^l & X_1 & c_1 & X_1 \times c_1 \\ 1 & x_{2,1} & y_{2,1} & \cdots & x_{2,1}^k y_{2,1}^l & X_1 & c_2 & X_1 \times c_2 \\ & \vdots & & & & \vdots & & \\ 1 & x_{n,m} & y_{n,m} & \cdots & x_{n,m}^k y_{n,m}^l & X_m & c_n & X_m \times c_n \end{pmatrix} \end{array} \tag{24}$$

where X_μ is the airmass of the νth image, and c_ν is the R-I colour of the νth star.

The least square solution for this set of linear equation can can be found as before as

$$\mathbf{p} = \mathbf{v} \cdot \mathbf{w}' \cdot \mathbf{u}^\mathbf{t} \cdot \mathbf{M}. \tag{25}$$

References

Chromey, F.R. & Hasselbacher, D.A. 1996, PASP, 108, 944

Harris, W.E. 1981, PASP, 93, 507

Møller, P., Järvinen, A., Rupprecht, G., Freudling, W., Patat, F., Romaniello, M., Ancker, M. V. D., Gotzens, M. P., Jehin, E., Mignani, R., O'Brien, K., Szeifert, T. 2005, "FORS: An assessment of obtainable photometric accuracy and outline of strategy for improvement (FORS IOT Secondary Standards Working Group)", VLT-TRE-ESO-13100-3808 (FWII)

Stetson, P.B. 2000, PASP, 112, 925

Stetson, P.B. 2006, fields listed at http://cadcwww.dao.nrc.ca/cadcbin/wdbi.cgi/astrocat/stetson/query

Press, H., Tukolsky, S.A., Vetterling, W.T. and Flannely, B.P., 1995, Numerical Recipes in Fortran: The Art of Scientific Computing, Cambridge University Press, pp.51ff

List of Figures